

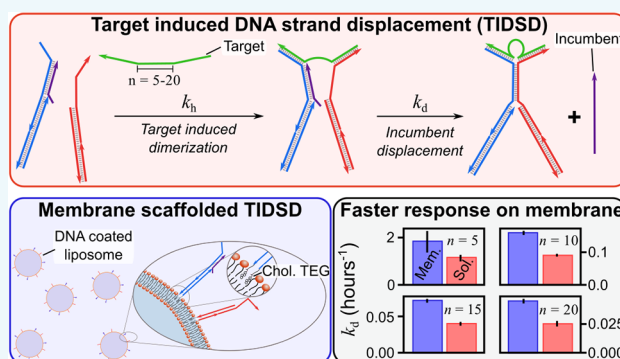
Membrane Scaffolds Enhance the Responsiveness and Stability of DNA-Based Sensing Circuits

Will T. Kaufhold, Ryan A. Brady, Joshua M. Tuffnell, Pietro Cicuta,^{1b} and Lorenzo Di Michele*^{1b}

Biological and Soft Systems, Cavendish Laboratory, University of Cambridge, JJ Thomson Avenue, Cambridge CB3 0HE, United Kingdom

Supporting Information

ABSTRACT: Target-induced DNA strand displacement is an excellent candidate for developing analyte-responsive DNA circuitry to be used in clinical diagnostics and synthetic biology. While most available technologies rely on DNA circuitry free to diffuse in bulk, here we explore the use of liposomes as scaffolds for DNA-based sensing nanodevices. Our proof-of-concept sensing circuit responds to the presence of a model target analyte by releasing a DNA strand, which in turn activates a fluorescent reporter. Through a combination of experiments and coarse-grained Monte Carlo simulations, we demonstrate that the presence of the membrane scaffold accelerates the process of oligonucleotide release and suppresses undesired leakage reactions, making the sensor both more responsive and robust.



INTRODUCTION

DNA has been abstracted from its cellular role in the storage of genetic information, and its base pairing interactions have been exploited to create a diverse range of self-assembling nanodevices and materials.^{1–5} The programmability of DNA association can be employed also to design chemical reaction networks, whose most ubiquitous mechanism is toehold-mediated strand displacement.^{6,7} In this reaction, hybridization of an invader single-stranded (ss) DNA molecule to a short toehold region on a substrate strand allows the invader to displace and release an incumbent strand initially bound to the substrate, after a period of reversible branch migration.^{6,7}

Target-induced DNA strand displacement (TIDSD) can be seen as a conceptual extension of the toehold mechanism, in which colocalization between substrate and invader is not mediated by base-pair complementarity, but by the presence of a target analyte.^{8–11} Both the invader and the substrate host a chemical modification or a DNA aptamer that can bind different epitopes on the analyte, whose presence thus causes the dimerization of the two DNA constructs. The latter then triggers the displacement of the incumbent. The released strand can finally be coupled to a downstream reaction cascade that signals the detection of the analyte, which has made TIDSD ideal for the development of DNA-based sensing platforms.^{8–11}

The analyte-induced dimerization process exploited in TIDSD to transduce chemical signals mimics a widely conserved mechanism of cell biology.¹² Indeed, a very diverse range of cellular processes are mediated by dimerization of soluble proteins induced by a specific analyte or ligand,

including physiological cell death as mediated by the Bcl-2 family of proteins¹³ and transcriptional control via ligand-activated transcription factors such as estrogen and progesterone.¹⁴ Very often the sensing machinery exploiting ligand-induced dimerization is confined to biological membranes. Examples include tyrosine kinase receptors,¹⁵ the TGF- β family of cytokines,¹⁶ and the T-cell receptor signaling pathways,¹⁷ all using a ligand to initiate transduction via the formation of homodimers or heterodimers of monomeric species.¹⁸ The variety of situations in which biological cells exploit this simple transduction mechanism follows from its applicability to a diverse range of targets, such as sterols, peptides, or even ions as in the case of cell adhesion mediation by E-cadherin induced by calcium.¹⁹ This remarkable versatility broadens the scope of biomimetic DNA-based sensing platforms relying on TIDSD, which have been shown to respond to targets such as streptavidin,⁸ various antibodies,^{9,10} and the HIV viral capsid.¹¹

Motivated by the effectiveness and ubiquity of membrane-bound biological receptors activated by analyte-induced dimerization, here we explore the possibility of optimizing the performance of DNA-based sensing devices relying on TIDSD by confining them to artificial lipid membranes. DNA constructs, here referred to as “receptors” to evoke the analogy

Special Issue: Interfacing Biology with Materials using DNA Assemblies

Received: January 31, 2019

Revised: March 6, 2019

Published: March 13, 2019

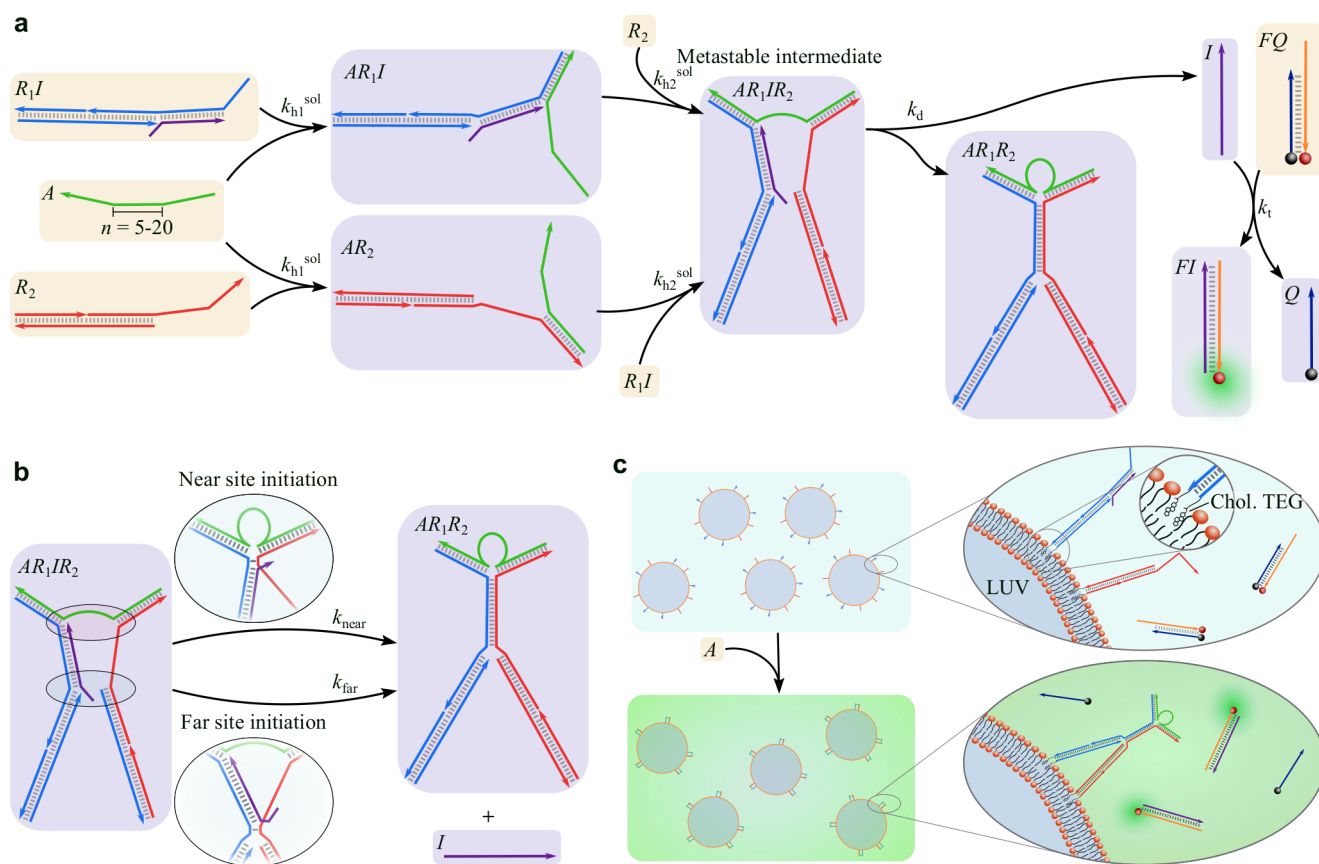


Figure 1. Implementation of DNA-based sensing platforms. (a) Kinetic pathway leading to analyte detection for the solution-based system as described by eqs 1–6. From left to right, analyte strand A leads to irreversible dimerization of receptor constructs R_1I and R_2 . Strand displacement results in the release of the incumbent strand I , which then displaces the quencher strand Q from the reporter construct FQ , leading to a detectable fluorescent signal. (b) Strand displacement can initiate at either end of the R_1I duplex region, labeled as *near* and *far* active sites. (c) Membrane-based sensing platform. Receptors identical to those of the solution-based system (a) can be grafted to the outer surface of LUVs through a double-cholesterol-TEG modification.

with their biological counterparts, are tethered to the outer leaflet of liposomes (large unilamellar vesicles, LUVs) by means of cholesterol modifications.^{20–23} In the presence of a target analyte, the synthetic DNA receptors dimerize and release an incumbent strand, triggering a downstream fluorescent response. For simplicity and generality, we consider target analytes consisting of ssDNA strands of various lengths, resulting in different degrees of colocalization in the dimerized receptors. We analyze the activation kinetics of the sensor through a combination of fluorimetry and coarse-grained Monte Carlo simulations, finding that confining the receptors to a membrane accelerates the process of strand release for all analytes. We show that the increased response rate follows from a greater probability of colocalization between the active sites where strand displacement is initiated.

The faster response of these membrane-scaffolded sensing platforms, as compared to solution-based circuits, is complemented by their comparatively leakage-free nature. Over a period of 70 h, our membrane-bound receptors demonstrated no discernible leakage, a feature the solution-based reaction networks do not share. These characteristics make the membrane-scaffolded networks excellent candidates for developing new diagnostic devices for generic biomarkers.

In addition to their biosensing potential, responsive liposomes are relevant in the context of bottom up synthetic biology as basic artificial cells,^{24,25} along the lines of recent

contributions by Rondelez and co-workers²⁶ and by de Greef and co-workers.²⁷ Indeed, reaction networks on or within these cell-like units may be interfaced in a modular fashion with other DNA-nanotechnology elements to process information analogously to an *in vivo* signal cascade,^{28,29} enabling complex life-like responses.^{30,31}

RESULTS AND DISCUSSION

Implementation. As illustrated in Figure 1a (left), the TIDSD receptors are experimentally implemented as two DNA constructs. One receptor, labeled as R_1 (blue), is initially hybridized to an incumbent DNA molecule, I (purple). The other DNA receptor, labeled as R_2 (red), features a single-stranded with the same sequence as I , which is thus thermodynamically capable of displacing the incumbent strand from receptor R_1 , forming a receptor-receptor heterodimer.

The rate of incumbent displacement depends on the relative concentration of R_1I , and R_2 , as strand-displacement reactions are known to be second order.⁷ For freely diffusing receptors in solution at typical experimental concentrations (nanomolar range), the absence of any mechanisms colocalizing the constructs makes incumbent displacement highly unlikely. The presence of the target analyte strand A (green in Figure 1), which binds to two 15-base domains on R_1I and R_2 , induces their dimerization and substantially increases their local concentration. We term the resulting AR_1R_2 structure the

metastable intermediate (Figure 1a, center), which is analogous to the three-strand intermediate in toehold-mediated strand displacement reactions,⁷ biotinylated DNA receptors dimerized by streptavidin,³² or DNA receptors dimerized by an antibody.⁹ The analyte-induced dimerization is effectively irreversible over experimental time scales.

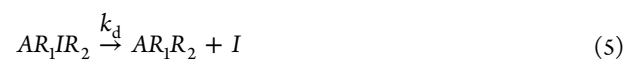
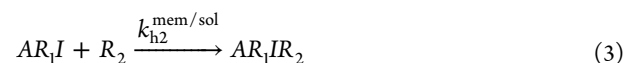
The process of incumbent-strand displacement is expected to initiate with occasional fraying of the complementary bonds between I and R_1 , occurring most frequently at a termination of the double-stranded region where base pairing is less stabilized by base stacking.^{6,7,33} This transient opening creates an opportunity for the competing DNA strand R_2 to bind at that location instead, initiating a process known as branch migration,^{34,35} where bonds are reversibly exchanged, here between R_1I and R_1R_2 . Branch migration is a stochastic process, often described as a one-dimensional (1D) random walk in a rugged free-energy landscape,^{6,7} that can either result in the system reverting to the metastable intermediate or progress until all possible R_1R_2 bonds are formed and the incumbent is released. As demonstrated by Figure 1b in our system, branch migration can initiate at either end of the double-stranded region binding R_1 and I . We term the location of initiation nearest the analyte as the near active site, and the other as the far active site. Branch migration is fast compared to the time scales associated with its initiation, whose kinetics are the limiting factor in the overall TIDSD reaction.³⁶

The entropic gain associated with the release of the incumbent makes the reverse reaction thermodynamically unfavorable, which is also kinetically hindered by the absence of any mechanism colocalizing I with the AR_1R_2 construct. Furthermore, the freed incumbent I is utilized to activate a fluorescent reporter circuit by displacing a quencher-bearing strand (Q) from a fluorophore-bearing strand (F) through toehold-mediated strand displacement (Figure 1a, right). The fluorescence of duplex FI can thus be monitored over time to track the progression of the TIDSD reaction. Note that all duplexes in the system are at least 15 base pairs long, making them irreversible over experimental time scales unless the strands involved are displaced by analyte- or toehold-induced strand displacement reactions.

Two versions of the detection platform are experimentally implemented, one with the receptors R_1I and R_2 freely dispersed in solution (“solution-based”, Figure 1a) and one in which the receptors are anchored to the outer surface of DOPC large unilamellar vesicles (LUVs) (“membrane-based”, Figure 1c). Irreversible anchoring is achieved through a double-cholesterol modification applied to a duplex region on the opposite side of the receptors compared to the analyte anchoring point (Figure 1c).^{21,22,37,38} Cholesterolized membrane-bound constructs are known to undergo free lateral diffusion across the fluid DOPC bilayer: even for large DNA origami tethered to a DOPC membrane by multiple cholesterol anchors, the diffusion coefficient of the constructs is in excess of $1 \mu\text{m}^2 \text{s}^{-1}$.³⁹ Noninteracting (inert) DNA constructs are present on the LUVs along with the receptors, to produce sufficient steric repulsion and stabilize the liposomes against nonspecific adhesion.²¹ Non-membrane-anchored receptors used for the solution-based platform are identical to the membrane-tethered ones, but lack the cholesterol moieties. All other components of the sensing circuit (A , FQ) are dispersed in solution for both the solution-based and the membrane-based implementations.

Unless specified otherwise, for each experiment aimed at characterizing the kinetics of the circuits’ response samples initially contained R_1I , R_2 , and FQ , each with bulk concentration of 20 nM, and A at 10 nM. The same concentrations were used for both the solution-based and membrane-based platforms. For the membrane-based system, the surface density of R_1I and R_2 on the liposomes is kept constant at $500 \mu\text{m}^{-2}$, and the concentration of LUVs is tuned to achieve an initial bulk concentration of the receptors equal to 20 nM. After mixing all components at time $t = 0$, we monitor the fluorescent emission of strand F over time. Analytes of four different lengths are tested, with a number n of free ssDNA thymine bases separating the two receptors equal to 5, 10, 15, and 20 (Figure 1a, left). All experiments are performed in near-physiological ionic strength (100 mM NaCl + 87 mM glucose + TE buffer). See Methods section for details on sample preparation and measurement protocols and SI for full information on the structure of the DNA constructs (Figure S1) and the sequences of their ssDNA components (Table S1).

Kinetic Pathway. The overall pathway is described by the following reactions, graphically summarized in Figure 1a



where eqs 1–4 describe the dimerization of the receptors induced by the analyte, eq 5 describes the strand-displacement process releasing I , and eq 6 describes the interaction of I with the reporter circuit.

The initial analyte-induced dimerization leading to the formation of the metastable intermediate is a two-step process, in which the analyte hybridizes with the two receptors sequentially. Each of the two steps is a second-order reaction with rate $k_{h1}^{\text{mem/sol}}$ and $k_{h2}^{\text{mem/sol}}$, respectively, where the superscripts distinguish between the membrane-based and solution-based systems. Hybridization rates of free oligonucleotides are most often assumed to be in the region of $10^6 \text{M}^{-1} \text{s}^{-1}$.⁷ However, a dependence on the viscosity and ionic strength of the solution has been reported in the literature.^{40,41} We measured the solution-phase hybridization rates experimentally (see Methods, SI, and Figure S2a), obtaining $k_{h1}^{\text{sol}} = k_{h2}^{\text{sol}} = (1.00 \pm 0.05) \times 10^5 \text{M}^{-1} \text{s}^{-1}$, compatible with values recorded at ionic strengths similar to those of our experiment.⁴¹

To model analyte-induced dimerization events on the liposomes, we make a distinction between the hybridization of the freely suspended analyte to the first membrane-anchored receptor, with rate k_{h1}^{mem} , and the on-membrane hybridization of this to the second receptor, with rate k_{h2}^{mem} . Previous reports

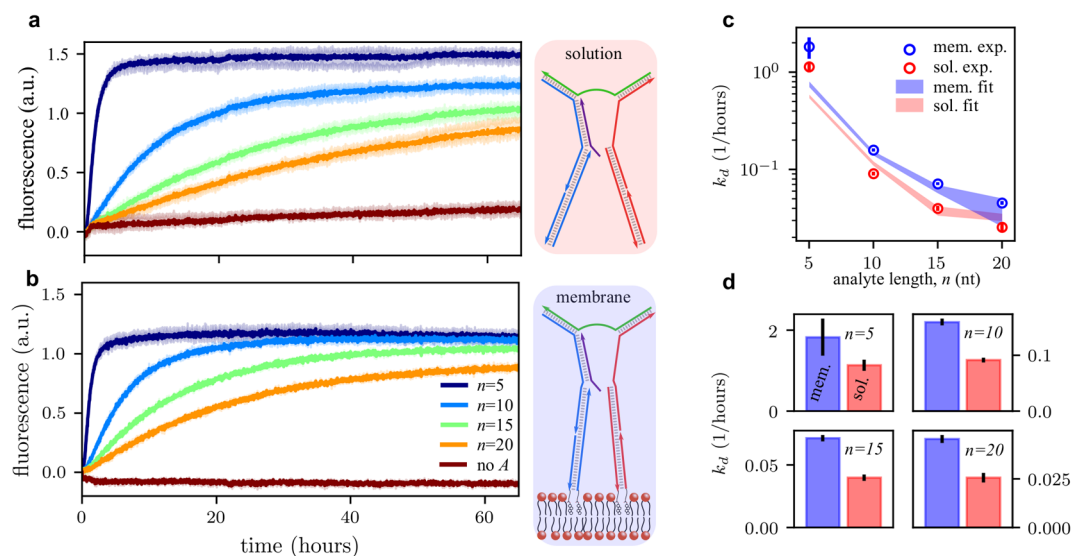


Figure 2. Membrane tethering speeds up analyte-sensing response. Fluorescent emission traces for analytes of different length (n), and negative-control experiment in the absence of A measured for the solution-based system (a) and the membrane-based system (b). Error bars are from the standard deviation over eight repeats for the solution-based system, and four repeats for the membrane-based system. (c) Experimental incumbent-strand release rate k_d derived from the data in panels a and b (symbols) and best global fits based on eqs 7–9 and on the numerical (MC) estimates of the effective active-site concentrations ρ_{near} and ρ_{far} (shaded regions). Error bars on the experimental data correspond to one numerically estimated standard deviation (see SI); those of the best fits are represented by the width of the curve and also correspond to one standard deviation. (d) Direct comparison of k_d values between the membrane-tethered and solution-based sensing platforms demonstrating a faster response rate in the former regardless on analyte length.

found reduced hybridization rates for DNA oligonucleotides when their complementaries are tethered to solid substrates.^{41–43} In the absence of experimental estimates of the rates of hybridization of oligomers to complementary ones tethered to fluid membranes, we chose to use for $k_{\text{h1}}^{\text{mem}}$ the same value measured for the bulk reactions ($k_{\text{h1}}^{\text{mem}} = (1.00 \pm 0.05) \times 10^5 \text{ M}^{-1} \text{ s}^{-1}$), being aware that this approximation provides an upper bound. Owing to the high effective concentration of tethered receptors on the membrane and their relatively high diffusivity,³⁹ we assume the second step of the analyte-induced dimerization (eqs 3 and 4) to be instantaneous as compared to all other processes, equivalent to $k_{\text{h2}}^{\text{mem}} \rightarrow \infty$. As a result, and given the effective irreversibility of analyte-receptor bonds, inter-LUV bridging events are kinetically inaccessible.²¹ Note that $k_{\text{h1}}^{\text{mem}/\text{sol}}$ and $k_{\text{h2}}^{\text{mem}/\text{sol}}$ are assumed to be independent of analyte length n .

The process of incumbent strand-displacement and release then follows first-order kinetics of rate constant k_d ⁸ (eq 5), while the toehold-mediated activation of the reporter circuit is best described as a second-order process with a rate constant k_t ^{6,7} (eq 6).

The rate k_t is conserved across implementations with different analyte lengths and free/membrane-bound receptors and could be experimentally estimated as $k_t = (2.6 \pm 0.3) \times 10^4 \text{ M}^{-1} \text{ s}^{-1}$ (see Methods, SI, and Figure S2b). Note that despite the long (7 nt) toehold between I and F , the toehold rate k_t in our system is still smaller than the free oligonucleotide hybridization rate, different from previous reports where the two are found to converge for toeholds with length ≥ 6 nt.^{6,7} We argue that such a difference could be a consequence of the lower ionic strength of our experiments reducing the hybridization free energy of the invader–toehold interactions. Furthermore, strand I can form a three base-pair

stem-loop motif when isolated, which may reduce the rate of Q-strand displacement.

Having made estimates of $k_{\text{h1}}^{\text{mem}/\text{sol}}$, $k_{\text{h2}}^{\text{mem}/\text{sol}}$ and k_v , we can then extract the incumbent-displacement rate k_d by fitting the time dependent fluorescent signal, proportional to the concentration of unquenched FI duplexes. Fitting is done using the numerical solutions of the coupled system of partial differential equations associated with the reaction pathway in eqs 1–6, as detailed in the SI.

Effect of Membrane Scaffold on the Rate of Incumbent Strand Release. Fluorescent emission traces in Figure 2 demonstrate the effect of changing analyte length n on the response rate of the system, for both the solution-based (Figure 2a) and the membrane-based implementations (Figure 2b). In both cases, the response becomes monotonically slower with increasing n . Given that $k_{\text{h1}}^{\text{mem}/\text{sol}}$, $k_{\text{h2}}^{\text{mem}/\text{sol}}$ and k_t are independent of analyte length, the system's response is dictated by the first-order rate of incumbent strand-displacement k_d , which drops by almost 2 orders of magnitude between $n = 5$ and $n = 20$ (Figure 2c).

The observed trends are readily explained as a consequence of the expected decrease in the effective concentration of active sites with increasing n and are fully consistent with a qualitatively similar system studied in solution by Genot et al.: the *remote-toehold*.³⁶ In this mechanism a toehold domain is separated from the location where branch migration initiates by a short single-stranded region; as this region increases in length the incumbent strand is released at a lower rate.³⁶

In Figure 2c,d we compare the experimental incumbent-release rates of the solution-based and membrane-based implementations, and, strikingly, we observe that the presence of the membrane results in larger values of k_d by a factor of between 1.3 ($n = 5$) and 1.8 ($n = 20$). Further, as the value of $k_{\text{h1}}^{\text{mem}}$ utilized here represents an upper bound, the value of k_d

determined for the membrane-based receptor can be seen as a lower bound, implying that membrane tethering may have an even larger accelerating effect on strand displacement than the one we estimate here.

Figure 2a,b also shows fluorescence traces of negative-control experiments performed in the absence of the analyte *A*. A slight increase in fluorescence is observed for the solution-based system, indicating a degree of leakage. Remarkably, no increase is observed for the membrane-based implementation. The comparatively leakage-free nature of the membrane-based sensing platform is further discussed below.

Coarse-Grained Numerical Simulations. To rationalize the effect of membrane-induced confinement on the rate of incumbent strand displacement, we perform Monte Carlo (MC) simulations on the metastable intermediates AR_1R_2 for all the implementations of the system tested in experiments. We utilize the coarse-grained DNA representation oxDNA, which models each nucleotide as three beads: a backbone site, a π -stacking site, and a hydrogen bonding site, interacting through six potential energy terms.^{45,46} The values for these potentials have been chosen through a top down parametrization approach to replicate thermodynamic and structural properties as determined by experiments.^{45,46} Here we utilize the updated version of the model, oxDNA2 that explicitly accounts for screened Coulomb interactions and better approximates the geometry of the double-helix by introducing major and minor grooves.⁴⁷ For membrane-bound receptors, the presence of the membrane is modeled implicitly through harmonic constraints, as detailed in the Methods section and graphically summarized in Figure 3a. Note that such a modeling choice results in fully flexible tethering points for the receptors that, in the absence of the mutual confinement induced by the analyte, would be able to pivot unimpeded around the (mobile) anchoring location. Although

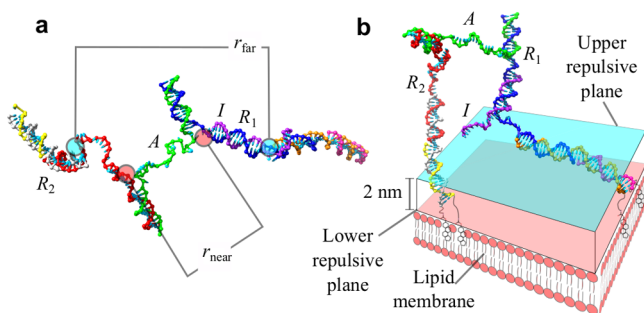


Figure 3. Coarse-grained modeling of the metastable intermediates enables estimation of the effective concentration of the active sites for initiation of strand displacement. Monte Carlo simulation snapshots of the metastable intermediates for the solution-based (a) and the membrane-based (b) systems. Far and near active sites for initiation of strand displacement are highlighted in panel (a) along with their distance, sampled in the simulations. For the membrane-based system (b), the presence of the membrane is encoded by repulsive harmonic planes: all nucleotides are forced to be above the lower plane (pink), while the cholesterolized nucleotides are confined between the latter and the upper plane (light blue). Sketches of the lipid membrane and the cholesterol-TEG modifications are included for illustration purposes and are not part of the simulation. The cholesterolized strands have been given alternate colors from Figure 1, to guide the eye in distinguishing them from the strands involved in the displacement process. Snapshots from simulation are visualized with UCSF Chimera.⁴⁴

the assumption of free pivoting has been broadly employed when modeling DNA constructs anchored to synthetic membranes,^{21–23,48} recent all-atom molecular dynamics simulations reported the possibility of preferential orientations, affected by multiple system-specific factors.⁴⁹ Nonetheless, for the sake of generality and in the absence of data relative to our experimental implementation, we chose not to constrain the rotational motion of the receptors.

Two Pathways for Displacement. The first-order rate constant k_d can be further described as a combination of rate constants representing displacement after initiation at the near and far active site

$$k_d = k_{\text{near}} + k_{\text{far}} \quad (7)$$

valid under the reasonable assumption that branch migration is highly unlikely to initiate simultaneously at both active sites.

In accordance with previous analysis, we conjecture that the rates of toehold-less displacement are proportional to the effective concentrations of active sites for branch-migration initiation³⁶ and define

$$k_{\text{near}} = \tilde{k}_{\text{near}} \rho_{\text{near}} \quad (8)$$

$$k_{\text{far}} = \tilde{k}_{\text{far}} \rho_{\text{far}} \quad (9)$$

where $\rho_{\text{near/far}}$ is the effective concentration of the near and far active sites and $\tilde{k}_{\text{near/far}}$ is the second-order rate coefficient.

MC simulations of the metastable intermediate are used to sample the distances r_{near} and r_{far} between the near and the far active sites (Figure 3a), which we then use to estimate $\rho_{\text{near/far}}$ as detailed in the Methods.

Figure 4a summarizes the dependence of $\rho_{\text{near/far}}$ on analyte length n for both membrane-tethered and free receptors. Interestingly, we observe that the effective concentration of the far active sites is nearly unaffected by n , while that of the near active sites drops exponentially with analyte length. Under the assumption that \tilde{k}_{near} and \tilde{k}_{far} are independent of analyte length, eqs 7, 8, and 9 suggest that a change in the likelihood of branch-migration initiation at the near active site is responsible for the observed n -dependence of k_d (Figure 2c).

Figure 4a, and more clearly Figure 4b, demonstrate how membrane-tethered receptors experience an increase in both ρ_{near} and ρ_{far} as compared to free constructs. This observation is fully consistent with the observed effect of membrane tethering on k_d , and thus offers a likely explanation for the accelerated response of the membrane-based sensing platform.

Rates of displacement are known to be contingent not only on the rate of initiation of branch migration, but heavily influenced by sequence identity, and ultimately the free-energy profile of branch migration.⁵⁰ Since these free-energy profiles will certainly be different between the far and near displacement pathways, we expect $\tilde{k}_{\text{near}} \neq \tilde{k}_{\text{far}}$. With the assumption that \tilde{k}_{near} and \tilde{k}_{far} are independent of analyte length n and unaffected by membrane tethering, we estimate the two coefficients by performing a global fitting of the experimentally determined values of k_d (Figure 2b) and utilizing the numerically derived ρ_{near} and ρ_{far} (Figure 4a). The fits reproduce reasonably well the experimental trends for k_d (Figure 2b) and render estimates of the two rate coefficients that are markedly different in magnitude, with $\tilde{k}_{\text{far}} \approx 7\tilde{k}_{\text{near}}$ (Figure 4c). The origin of the observed asymmetry may lay in the presence of a 5' overhang in the incumbent strand *I* at the

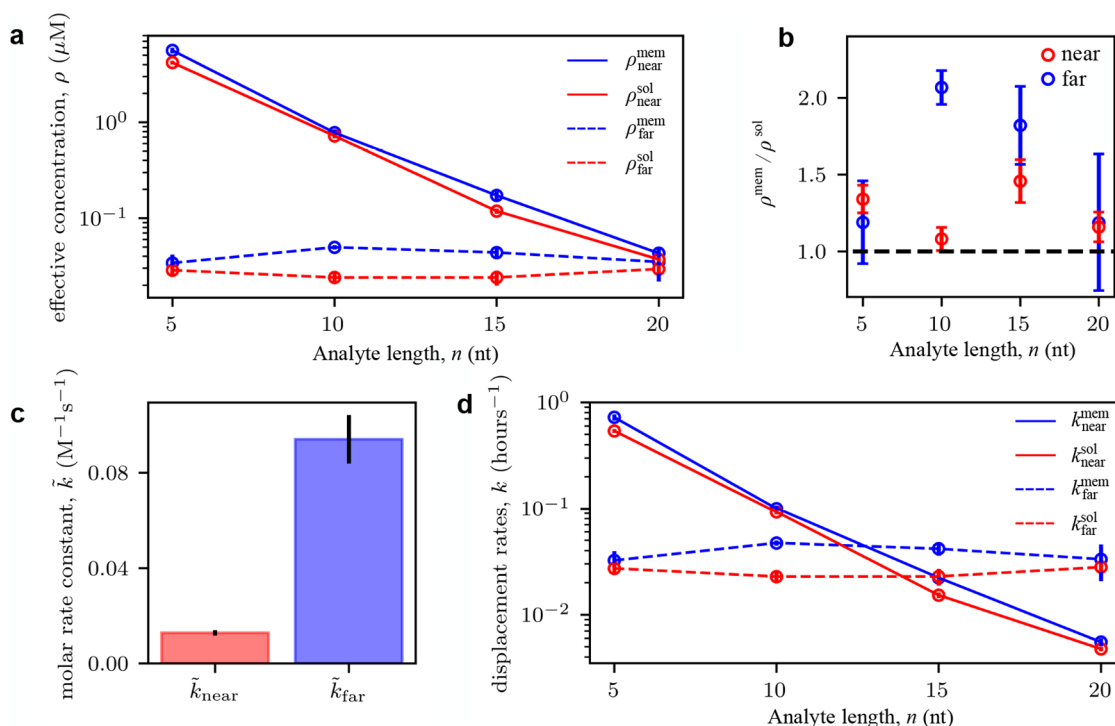


Figure 4. Effective concentration of active sites depends on membrane tethering and analyte length. (a) Effective concentrations for the near active sites (ρ_{near} , solid lines) and the far active sites (ρ_{far} , dashed lines) as a function of analyte length n as estimated from MC simulations. Data relative to the solution-based system are shown in red, and those relative to the membrane-tethered system are in blue. Error bars are estimated as discussed in the Methods. (b) Ratio between the near- and far-site effective concentrations shown in panel (a). (c) Second-order rate constants \tilde{k}_{near} and \tilde{k}_{far} for initiation of strand displacement at the near and far active sites respectively, as determined from the fits in Figure 2b (see eqs 7–9). (d) Dependence of the corresponding first-order rates k_{near} and k_{far} on n (eq 7).

location of the far active site. It has been previously observed that “inert tails” such as this overhang have the capacity of destabilizing duplexes in moderate ionic strength conditions, such as those of the present experiment.⁵¹ We speculate that the overhang might aid the initiation of the branch-migration process by lowering the free-energy barrier for the formation of the first base-pairing bonds between the two receptors R_1 and R_2 , for instance by enhancing fraying of the R_1I duplex at the far active site.

Figure 4d shows the estimates of the first-order rates of displacement for the near and far pathways, k_{near} and k_{far} , as derived using eqs 8 and 9. As a result of the strong suppression of ρ_{near} with increasing n the two rates show a crossover point as a function of analyte length: if short analytes are used, displacement is more likely to occur at the near site, while long analytes favor the far-site pathway.

Leakage Reduction. Toehold-less strand-displacement reactions can over time result in the release of incumbent strands even in the absence of the analyte. This process, known as leakage, results in false-positive fluorescent signals and may reduce the shelf life of biosensing kits based on TIDSD.

As highlighted by the negative controls in Figure 2a,b, in experimental conditions relevant to the results discussed this far, leakage is limited over experimental time scales (up to 70 h), and even absent for the membrane-based system.

To better assess the effect of membrane tethering on leakage, we thus perform negative-control experiments after increasing the concentration of R_1I and R_2 , along with that of the reporter element FQ , by a factor of 5 resulting in an overall bulk concentration of 100 nM. Notably, for the membrane-based system, this is done by utilizing a 5× higher

concentration of LUVs, while leaving unchanged the surface density of membrane-tethered receptors. As expected, the more concentrated systems display a non-negligible rate of leakage, but still the membrane-based implementation appears to be significantly more resilient in comparison to the solution-based one (Figure 5).

In our system, leakage can potentially occur via two independent pathways. One pathway initiates with a toehold-less strand-displacement reaction between R_1I and R_2 occurring without the formation of the metastable intermediate

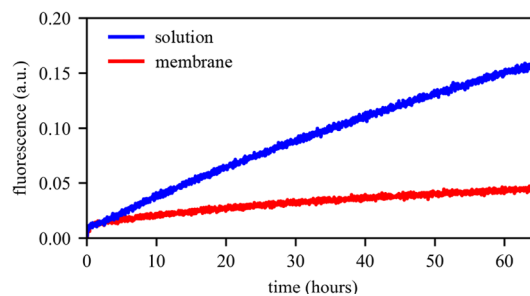


Figure 5. Membrane tethering suppresses leakage. Fluorescence-emission curves for negative-control leakage experiments performed in the absence of analyte strand A at 5× concentration of all components for the solution-based and membrane-based systems (100 nM). Note that for the membrane-based system a higher receptor concentration is achieved by increasing the concentration of liposomes while keeping the surface density of tethered receptors constant.

The released incumbent strand then activates the reporter circuit as described by eq 6. The second pathway is independent of the presence of R_2 and produces a fluorescent signal via a toehold-less strand-displacement reaction between R_1I and FQ



For the membrane-based system, the pathway described by eq 10 relies on interactions between tethered receptors, which may be influenced by factors such as membrane-induced orientational constraints,⁴⁹ or steric hindrance produced by the presence of tethered inert DNA constructs. These effects might result in a slow down of the reaction in eq 10. Furthermore, we note that for the membrane-based platform analyte-less R_1I - R_2 reactions are most likely to occur between receptors tethered to the same liposome rather than across different LUVs. Thus, we expect the reaction pathway in eq 10 to be weakly affected by increasing the overall bulk concentration of R_1I and R_2 , as long as their surface density on the liposomes remains constant.

Similarly, the leakage pathway described in eq 11 relies on interactions between a membrane-tethered (R_1I) and a free construct (FQ), which may be slower than the corresponding reactions occurring between two soluble elements,^{41–43} reducing leakage rate.

CONCLUSION

Through a series of proof-of-concept experiments and computer simulations, we have demonstrated that membrane scaffolding provides a mechanism to enhance TIDSD, both accelerating responsiveness and suppressing leak reactions.

Membrane tethering of the sensing DNA constructs increases the effective concentration of the active sites for initiation of branch migration, which leads to a higher rate of incumbent-strand displacement and ultimately to an overall faster response of the system to the presence of the target analyte. The increase in response rate occurs regardless on analyte size, and thus on the degree of confinement it imposes between the two receptors.

Receptor-functionalized liposomes demonstrate substantially more stability than their free in solution analogues, being leak-free on time periods of at least 70 h.

These factors make liposome scaffolded TIDSD optimal for the development of new diagnostic tools in a clinical setting.^{8–11} The receptor functionalized liposomes can also be regarded as simple cell-like agents able to exchange information with the local chemical environment, a starting point for the development of synthetic cell consortia in the context of bottom-up synthetic biology.^{26,27}

METHODS

Materials. DNA. Sequences of the reporter circuit were taken from ref 8. Remaining sequences were reverse-engineered to interact with that reporter circuit using the NUPACK design tool.⁵² The sequences of all the strands used are shown in SI, Table S1, while the detailed structure is shown in Figure S1. 5'-Cholesteryl-modified DNA strands were purchased from Eurogentec (Liege, Belgium) with high performance liquid chromatography (HPLC) purification. All other DNA strands were purchased from Integrated DNA Technologies (Coralville, Iowa, United States) also purified by

HPLC. Strand F was modified with 6-FAM (Fluorescein). Q was modified with Iowa Black.

Lipids and Buffers. Sodium chloride (BioUltra, >99.5%), D-(+)-glucose (>99.5%), 100× TrisEDTA buffer, and sucrose were purchased from Sigma-Aldrich. 1,2-Dioleoyl-*sn*-glycero-3-phosphocholine (DOPC, >99%) was purchased from Avanti Polar Lipids Inc. (Alabaster, Alabama, USA). Texas-Red-tagged 1,2-dihexadecanoyl-*sn*-glycero-3-phosphoethanolamine, triethylammonium salt (TX-DHPE) was purchased from ThermoFisher Scientific (Waltham, Massachusetts, USA).

Experimental Methods. DNA Handling. DNA was shipped lyophilized and was reconstituted to a concentration of approximately 100 μM in TE buffer (1 mM EDTA, 10 mM Tris, pH 8.0). Buffers were filtered through 0.22 μm pore poly(ether sulfone) filters (Millex) prior to use. Absorbance of the stock solutions at 260 nm was evaluated by UV-vis spectrophotometry on a Thermo Scientific NanoDrop 2000. The concentrations of the stock solutions were evaluated by the ratio of the absorbance at 260 nm to the extinction coefficient of the DNA. Stock solutions were subsequently stored frozen at -20°C .

DNA Hybridization. Assembly of multistranded DNA constructs, namely, R_1I , R_2 , FQ and inert constructs (see SI, Figure S1 and Table S1), was facilitated by thermal annealing. For each construct, all single-stranded components were combined at equal concentrations of 2 μM in 100 mM NaCl TE buffer, with the only exception of FQ , where a 50% excess of Q was used (F - Q molar ratio of 2:3). The annealing process was carried out on a Techne TC-512 thermocycler. The strands were heated to 90°C for 5 min to ensure all DNA was melted and cooled steadily to 4°C over 3 h.

LUV Synthesis. DOPC large unilamellar vesicles (LUVs) were formed via extrusion, as detailed in previous reports.⁵³ Briefly, 220 μL of DOPC solution in chloroform (25 mg mL^{-1} , Avanti Polar Liquids) was added to a glass vial and desiccated under a vacuum. The DOPC film then was rehydrated in 500 μL of 300 mM sucrose in Milli-Q water by vortexing and freeze thawed under liquid nitrogen four times. The resultant suspension was extruded using a mini extruder kit (Avanti Polar Liquids) through a polycarbonate membrane pore (Whatman) of pore size 1.0 μm . LUVs were stored at room temperature and used within 3 days.

Functionalizing LUVs with DNA. LUVs were functionalized by incubation with cholesterolized DNA constructs in a solution of 100 mM NaCl + 87 mM glucose TE buffer for 24 h at room temperature. The osmolarity of this solution was chosen to match the osmolarity of the liposomes to prevent osmotic-shock-induced rupture. During incubation, the concentration of lipids and DNA was kept to 5× the eventual concentration in the final samples. The ratio of LUVs to cholesterolized receptors was chosen for the eventual surface concentration of each receptor type, R_1I and R_2 , to be one per 2000 nm^2 (surface density 500 μm^{-2}). Calculation of the surface density of DNA was performed by assuming 100% efficiency of LUV synthesis, and an average area per DOPC headgroup of 72.5 \AA .⁵⁴ Additional “inert” cholesterolized double-stranded DNA (dsDNA) was added to increase the total surface concentration of DNA to one strand every 500 nm^2 (including R_1I , R_2 and inert strands). A higher surface coverage was required to provide sufficient steric repulsion between the liposomes and prevent their aggregation as confirmed by confocal microscopy.²¹ The design of the inert strands is shown in the SI, Figure S1.

To verify that incubation leads to adherence of the cholesterolized nanostructures to the membrane, the protocol was repeated using LUVs made fluorescent through a 10% molar fraction of TX-DHPE. After the 24-h incubation, the DNA intercalating dye Sybr Safe (Sigma-Aldrich) was added to the sample. Fluorescent signal was measured at 596 nm/616 nm (excitation/emission, Texas Red) and 485 nm/515 nm (Sybr Safe) using a Cary Eclipse fluorimeter. The solution was then centrifuged at 8000 rcf for 30 min to sediment the vesicles before measuring the fluorescence of the supernatant. We observed 90% cosegregation of the Sybr Safe signal (corresponding to DNA) with the Texas Red signal (corresponding to the LUVs), indicating that the vast majority of the DNA was indeed grafted to the liposomes. To remove any DNA not adhering to the vesicles, after the incubation process, functionalized vesicles were centrifuged for 30 min at 1000 rcf, and the eluent discarded and replaced with fresh buffer. Vesicles were then resuspended by gently pipetting up and down until the pellet had vanished.

Fluorescence Kinetic Assays. For both the solution-based and the membrane-based sensors, reactions aimed at characterizing the kinetics of their response were performed at 100 μL volume in a 96-well plate (Grenier 96 well F-bottom) in a solution of 100 mM NaCl, 87 mM glucose TE buffer. For the solution-based system, samples initially contained 20 nM FQ , 20 nM R_1I , 20 nM R_2 , 10 nM A , 10 nM Q , and 1 μM 20 nt-long polyT. The excess Q results from the concentration mismatch of the two components in the preparation of FQ and does not affect the kinetic response of the system. Samples for testing the membrane-based platform contained the same components, except that R_1I and R_2 were replaced by a suitable concentration of receptor-functionalized vesicles, calculated to achieve the same overall concentration of receptors of the free-receptor case. The purpose of the polyT was to reduce nonspecific adsorption of DNA constructs to the walls of the well plate.

Fluorescence was monitored at 485 nm/520 nm for 70 h with a Fluostar Omega (BMG Labtech), using a cycle time of 120 s, with 100 flashes per well (bottom optic), and 1 s of 100 Hz vibration between cycles to ensure a well mixed system. The measurements were started within 2 min of mixing all the components. Within the first few minutes of control experiments with only 20 nM FQ , there is a small (~ 0.1 a.u.) decline in observed fluorescence, followed by no change over the subsequent 70 h. To control for this effect, we reduce each of the time varying fluorescence traces by a control experiment containing only 20 nM FQ , and 1 μM polyT. Initially there is substantial nonuniform fluorescence across different wells. To account for this, we reduce the fluorescence traces by the first measured value. Measurements were repeated eight times for each analyte length for the solution-based system and four times for the membrane-based system.

Determining $k_{\text{hl}/2}^{\text{mem}/\text{sol}}$ and k_t . The bulk oligonucleotide-hybridization rate used to approximate $k_{\text{hl}/2}^{\text{mem}/\text{sol}}$ was determined through a dedicated absorbance experiment. The second-order rate constant k_t describing the activation of the reporter circuit was determined through positive-control samples with I and FQ . Full details are reported in the SI text and Figure S2.

Extracting k_d . Using the estimates of $k_{\text{hl}/2}^{\text{mem}/\text{sol}}$ and k_t , we determined k_d by fitting experimental fluorescence curves for

each of the tested conditions with the numerical outcomes of eqs 1–6, under the assumption that the fluorescent signal is proportional to the concentration of the FI (eq 6). Uncertainty on the k_d parameter was extracted via a bootstrap resampling mechanism. Full details are provided in the SI.

Monte Carlo Simulations. Encoding the Effect of the Membrane. oxDNA has been parametrized only for DNA. To examine the effect of confinement on the distribution of conformations of the metastable intermediate for the membrane-bound case, the membrane was modeled implicitly through harmonic constraints. A lower repulsive plane (pink in Figure 3b) confines all particles to be above it, encoding the steric effect of the membrane. Two nanometers above this, an upper repulsive plane (light blue in Figure 3b) is applied to the four cholesterolized nucleotides, encoding for the presence of the TEG-cholesterol linker and limiting diffusion of the cholesterolized strands away from the membrane. To identify if the simulation results were contingent on the distance between the planes, simulations were performed also using a constraint of 1 nm, which resulted in negligible differences.

Initialization. The following mechanism was used to generate structures corresponding to the metastable intermediates for the cases of membrane-bound and free receptors. DNA strands were first initialized at random locations, and then, via a custom-made Python script, harmonic traps were introduced between nucleotides that would be paired in the final structure, forcing the system to relax into the sought configuration. Without these traps, which were removed after initialization, the computation time taken for the strands to form the expected structure is prohibitively long. This initial assembly was performed using Virtual Move Monte Carlo (VMMC),⁵⁵ with maximum cluster size equal to the entire system. During initialization, the monovalent salt concentration was set artificially high to minimize repulsion and accelerate Watson–Crick bond formation. Typical configurations of the metastable intermediates are illustrated in Figure 2.

Running Simulations. Once formed, the metastable intermediate was sampled using VMMC.⁵⁵ The temperature of the system was set to 27 $^\circ\text{C}$, and a monovalent salt concentration was set to 0.1 M, in line with experiments. The salt concentration affects only screening of the repulsion between the phosphate backbones, under a mean field Debye–Huckel treatment. To enhance sampling of the regions of the configuration space where the active sites are close, simulations were biased. For each metastable intermediate, separate simulations were run with a biasing potential between the near active sites and between the far active sites, with form $U_{\text{bias}} = r^2 0.0692 k_B T$, where $r = r_{\text{far}}$ or r_{near} . An ensemble of 64 metastable intermediates for each system were simulated for 10 h from the same initial configuration. Snapshots of the system were stored every 100 cluster moves. The time taken for equilibration and the statistical inefficiency of sampling the observable, $r_{\text{near}/\text{far}}$ were estimated through a recently developed method implemented in the Python package *pymbar*.⁵⁶ The number of independent samples acquired in the simulation varied between 1000 and 16 000 depending on the system in question.

Postprocessing. Trajectories were postprocessed using custom Python scripts to extract the distances between the active sites, $r_{\text{near}/\text{far}}$ (Figure 3a). The probability for the

distances between the active sites to be within a given limit r_{\max} was then estimated as

$$p(r_{\text{near/far}} < r_{\max}) = \frac{\int_0^{r_{\max}} p(r)_{\pi} e^{U_{\text{bias}}(r)\beta} dr}{\int_0^{\infty} p(r)_{\pi} e^{U_{\text{bias}}(r)\beta} dr} \quad (12)$$

where $p(r_{\text{near/far}})_{\pi}$ is the biased probability, extracted directly for the distribution of active site distance (for brevity we omit the subscript near/far in the right-hand side of eq 12). To estimate the bootstrapped uncertainties of $p(r_{\text{near/far}} < r_{\max})$, the subsampled probability distribution was resampled (50 replacements), and for each resampling, $p(r_{\text{near/far}} < r_{\max})$ acquired through the bias correction procedure. The uncertainty as used here is from the standard deviation of the resampled values. The probability $p(r_{\text{near/far}} < r_{\max})$ was then converted to an effective concentration of the active sites as

$$\rho_{\text{near}} = \frac{p(r_{\text{near}} < r_{\max})}{V_{\max}} \quad (13)$$

$$\rho_{\text{far}} = \frac{p(r_{\text{far}} < r_{\max})}{V_{\max}} \quad (14)$$

where $V_{\max} = 4/3\pi r_{\max}^3$ and r_{\max} is the minimum distance where our model is accurate, set to 3.5 nm. Using the numerically generated values of ρ_{near} and ρ_{far} for all receptor types and analyte lengths, in combination with eqs 7, 8, and 9 we obtain a two-parameter family of curves in which \tilde{k}_{far} and \tilde{k}_{near} are unknown and can be determined by fitting this family of curves to the 12 data sets of experimental rates k_d , 4 for membrane-bound systems, 8 for solution-based systems (corresponding to independent repeats). Fitting is performed using minimization of χ^2 , where the uncertainties for each data point are given by combined experimental uncertainties in k_d and simulation uncertainties in ρ_{near} and ρ_{far} .

■ ASSOCIATED CONTENT

Supporting Information

The Supporting Information is available free of charge on the ACS Publications website at DOI: 10.1021/acs.bioconjchem.9b00080.

Structure of the DNA constructs, DNA sequences, estimation of kinetic rates and numerical methods (PDF)

■ AUTHOR INFORMATION

Corresponding Author

*E-mail: ld389@cam.ac.uk.

ORCID

Pietro Cicuta: 0000-0002-9193-8496

Lorenzo Di Michele: 0000-0002-1458-9747

Notes

The authors declare no competing financial interest.

■ ACKNOWLEDGMENTS

L.D.M. and P.C. acknowledge support from the EPSRC Programme Grant CAPITALS No. EP/J017566/1. L.D.M. acknowledges support from the Leverhulme Trust and the

Isaac Newton Trust through an Early Career Fellowship (ECF-2015-494) and from the Royal Society through a University Research Fellowship (UF160152). J.M.T. and R.A.B. acknowledge support from the EPSRC CDT in Nanoscience and Nanotechnology (NanoDTC), Grant No. EP/L015978/1. W.T.K. acknowledges support from an EPSRC DTP studentship. This work was performed using the Darwin Supercomputer of the University of Cambridge High Performance Computing Service (<http://www.hpc.cam.ac.uk/>), provided by Dell Inc. using Strategic Research Infrastructure Funding from the Higher Education Funding Council for England and funding from the Science and Technology Facilities Council. All the data needed to support and reproduce these results are presented within the paper and SI.

■ REFERENCES

- (1) Rothmund, P. W. K. (2006) Folding DNA to create nanoscale shapes and patterns. *Nature* 440, 297–302.
- (2) Seeman, N. C. (2007) An overview of structural DNA nanotechnology. *Mol. Biotechnol.* 37, 246–57.
- (3) Seeman, N. C., and Sleiman, H. F. (2017) DNA nanotechnology. *Nat. Rev. Mater.* 3, 17068.
- (4) Brady, R. A., Brooks, N. J., Cicuta, P., and Di Michele, L. (2017) Crystallization of Amphiphilic DNA C-Stars. *Nano Lett.* 17, 3276–3281.
- (5) Brady, R. A., Brooks, N. J., Foderà, V., Cicuta, P., and Di Michele, L. (2018) Amphiphilic-DNA Platform for the Design of Crystalline Frameworks with Programmable Structure and Functionality. *J. Am. Chem. Soc.* 140, 15384–15392.
- (6) Srinivas, N., Ouldrige, T. E., Šulc, P., Schaeffer, J. M., Yurke, B., Louis, A. A., Doye, J. P. K., and Winfree, E. (2013) On the biophysics and kinetics of toehold-mediated DNA strand displacement. *Nucleic Acids Res.* 41, 10641–10658.
- (7) Zhang, D. Y., and Winfree, E. (2009) Control of DNA Strand Displacement Kinetics Using Toehold Exchange. *J. Am. Chem. Soc.* 131, 17303–17314.
- (8) Li, F., Tang, Y., Traynor, S. M., Li, X.-F., and Le, X. C. (2016) Kinetics of Proximity-Induced Intramolecular DNA Strand Displacement. *Anal. Chem.* 88, 8152–8157.
- (9) Engelen, W., Meijer, L. H. H., Somers, B., de Greef, T. F. A., and Merckx, M. (2017) Antibody-controlled actuation of DNA-based molecular circuits. *Nat. Commun.* 8, 14473.
- (10) Ranallo, S., Prévost-Tremblay, C., Idili, A., Vallée-Bélisle, A., and Ricci, F. (2017) Antibody-powered nucleic acid release using a DNA-based nanomachine. *Nat. Commun.* 8, 15150.
- (11) Porchetta, A., Ippodrino, R., Marini, B., Caruso, A., Caccuri, F., and Ricci, F. (2018) Programmable Nucleic Acid Nanoswitches for the Rapid, Single-Step Detection of Antibodies in Bodily Fluids. *J. Am. Chem. Soc.* 140, 947–953.
- (12) Klemm, J. D., Schreiber, S. L., and Crabtree, G. R. (1998) Dimerization as a regulatory mechanism in signal transduction. *Annu. Rev. Immunol.* 16, 569–592.
- (13) Reed, J. C., Miyashita, T., Krajewski, S., Takayama, S., Aime-Sempe, C., Kitada, S., Sato, T., Wang, H. G., Harigai, M., Hanada, M., Krajewska, M., Kochel, K., Millan, J., and Kobayashi, H. (1996) Bcl-2 family proteins and the regulation of programmed cell death in leukemia and lymphoma. *Cancer Treat. Res.* 84, 31–72.
- (14) Tsai, M.-j., and O'Malley, B. W. (1994) Molecular mechanisms of action of steroid/thyroid receptor superfamily members. *Annu. Rev. Biochem.* 63, 451–486.
- (15) Heldin, C.-H. (1995) Dimerization of cell surface receptors in signal transduction. *Cell* 80, 213–223.
- (16) Massagué, J. (1996) TGF β signaling: Receptors, transducers, and mad proteins. *Cell* 85, 947–950.
- (17) Weiss, A., and Littman, D. R. (1994) Signal transduction by lymphocyte antigen receptors. *Cell* 76, 263–274.

- (18) Sako, Y., Minoghchi, S., and Yanagida, T. (2000) Single-molecule imaging of EGFR signalling on the surface of living cells. *Nat. Cell Biol.* 2, 168–172.
- (19) Nagar, B., Overduin, M., Ikura, M., and Rini, J. M. (1996) Structural basis of calcium-induced E-cadherin rigidification and dimerization. *Nature* 380, 360–364.
- (20) Beales, P. A., and Vanderlick, T. K. (2007) Specific binding of different vesicle populations by the hybridization of membrane-anchored DNA. *J. Phys. Chem. A* 111, 12372–12380.
- (21) Parolini, L., Kotar, J., Di Michele, L., and Moggetti, B. M. (2016) Controlling Self-Assembly Kinetics of DNA-Functionalized Liposomes Using Toehold Exchange Mechanism. *ACS Nano* 10, 2392–2398.
- (22) Bachmann, S. J., Kotar, J., Parolini, L., Saric, A., Cicuta, P., Di Michele, L., and Moggetti, B. M. (2016) Melting transition in lipid vesicles functionalised by mobile DNA linkers. *Soft Matter* 12, 7804–7817.
- (23) Parolini, L., Moggetti, B. M., Kotar, J., Eiser, E., Cicuta, P., and Di Michele, L. (2015) Volume and porosity thermal regulation in lipid mesophases by coupling mobile ligands to soft membranes. *Nat. Commun.* 6, 5948.
- (24) Trantidou, T., Friddin, M., Elani, Y., Brooks, N. J., Law, R. V., Seddon, J. M., and Ces, O. (2017) Engineering Compartmentalized Biomimetic Micro- and Nanocontainers. *ACS Nano* 11, 6549–6565.
- (25) Buddingh', B. C., and van Hest, J. C. M. (2017) Artificial Cells: Synthetic Compartments with Life-like Functionality and Adaptivity. *Acc. Chem. Res.* 50, 769–777.
- (26) Gines, G., Zadorin, A. S., Galas, J. C., Fujii, T., Estevez-Torres, A., and Rondelez, Y. (2017) Microscopic agents programmed by DNA circuits. *Nat. Nanotechnol.* 12, 351–359.
- (27) Joesaar, A., Yang, S., Bogels, B., van der Linden, A., Kumar, P., Dalchau, N., Phillips, A., Mann, S., de Greef, T., and Pieters, p. (2019) Distributed DNA-based Communication in Populations of Synthetic Protocells. *Nat. Nanotechnol.*, DOI: 10.1038/s41565-019-0399-9.
- (28) Montagne, K., Plasson, R., Sakai, Y., Fujii, T., and Rondelez, Y. (2011) Programming an in vitro DNA oscillator using a molecular networking strategy. *Mol. Syst. Biol.* 7, 466.
- (29) Padirac, A., Fujii, T., and Rondelez, Y. (2012) Bottom-up construction of in vitro switchable memories. *Proc. Natl. Acad. Sci. U. S. A.* 109, E3212–20.
- (30) Amir, Y., Ben-Ishay, E., Levner, D., Ittah, S., Abu-Horowitz, A., and Bachelet, I. (2014) Universal computing by DNA origami robots in a living animal. *Nat. Nanotechnol.* 9, 353–357.
- (31) Groves, B., Chen, Y.-J., Zurla, C., Pochekaïlov, S., Kirschman, J. L., Santangelo, P. J., and Seelig, G. (2016) Computing in mammalian cells with nucleic acid strand exchange. *Nat. Nanotechnol.* 11, 287–294.
- (32) Li, F., Zhang, H., Wang, Z., Li, X., Li, X.-F., and Le, X. C. (2013) Dynamic DNA Assemblies Mediated by Binding-Induced DNA Strand Displacement. *J. Am. Chem. Soc.* 135, 2443–2446.
- (33) Zgarbová, M., Otyepka, M., Šponer, J., Lankaš, F., and Jurečka, P. (2014) Base Pair Fraying in Molecular Dynamics Simulations of DNA and RNA. *J. Chem. Theory Comput.* 10, 3177–3189.
- (34) Radding, C. M., Beattie, K. L., Holloman, W. K., and Wiegand, R. C. (1977) Uptake of homologous single-stranded fragments by superhelical DNA: IV. Branch migration. *J. Mol. Biol.* 116, 825–839.
- (35) Green, C., and Tibbetts, C. (1981) Reassociation rate limited displacement of DNA strands by branch migration. *Nucleic Acids Res.* 9, 1905–18.
- (36) Genot, A. J., Zhang, D. Y., Bath, J., and Turberfield, A. J. (2011) Remote Toehold: A Mechanism for Flexible Control of DNA Hybridization Kinetics. *J. Am. Chem. Soc.* 133, 2177–2182.
- (37) Pfeiffer, I., and Höök, F. (2004) Bivalent Cholesterol-Based Coupling of Oligonucleotides to Lipid Membrane Assemblies. *J. Am. Chem. Soc.* 126, 10224–10225.
- (38) Beales, P. A., and Vanderlick, T. K. (2009) Partitioning of Membrane-Anchored DNA between Coexisting Lipid Phases. *J. Phys. Chem. B* 113, 13678–13686.
- (39) Czogalla, A., Franquelim, H. G., and Schwille, P. (2016) DNA Nanostructures on Membranes as Tools for Synthetic Biology. *Biophys. J.* 110, 1698–1707.
- (40) Wetmur, J. G., and Davidson, N. (1968) Kinetics of renaturation of DNA. *J. Mol. Biol.* 31, 349–370.
- (41) Gao, Y., Wolf, L. K., and Georgiadis, R. M. (2006) Secondary structure effects on DNA hybridization kinetics: a solution versus surface comparison. *Nucleic Acids Res.* 34, 3370–3377.
- (42) Henry, M. R., Wilkins Stevens, P., Sun, J., and Kelso, D. M. (1999) Real-Time Measurements of DNA Hybridization on Micro-particles with Fluorescence Resonance Energy Transfer. *Anal. Biochem.* 276, 204–214.
- (43) Sekar, M. M. A., Bloch, W., and St John, P. M. (2005) Comparative study of sequence-dependent hybridization kinetics in solution and on microspheres. *Nucleic Acid Res.* 33, 366–375.
- (44) Pettersen, E., Goddard, T., Huang, C. C., Couch, G., Greenblatt, D., Meng, E. C., and Ferrin, T. E. (2004) UCSF Chimera—a visualization system for exploratory research and analysis. *J. Comput. Chem.* 25, 1605–12.
- (45) Ouldrige, T. E., Louis, A. A., and Doye, J. P. K. (2010) DNA Nanotweezers Studied with a Coarse-Grained Model of DNA. *Phys. Rev. Lett.* 104, 178101.
- (46) Ouldrige, T. E., Louis, A. A., and Doye, J. P. K. (2011) Structural, mechanical, and thermodynamic properties of a coarse-grained DNA model. *J. Chem. Phys.* 134, 085101.
- (47) Snodin, B. E. K., Randisi, F., Mosayebi, M., Šulc, P., Schreck, J. S., Romano, F., Ouldrige, T. E., Tsukanov, R., Nir, E., Louis, A. A., and Doye, J. P. K. (2015) Introducing improved structural properties and salt dependence into a coarse-grained model of DNA. *J. Chem. Phys.* 142, 234901.
- (48) Shimobayashi, S. F., Moggetti, B. M., Parolini, L., Orsi, D., Cicuta, P., and Di Michele, L. (2015) Direct measurement of DNA-mediated adhesion between lipid bilayers. *Phys. Chem. Chem. Phys.* 17, 15615–15628.
- (49) Arnott, P. M., Joshi, H., Aksimentiev, A., and Howorka, S. (2018) Dynamic Interactions between Lipid-Tethered DNA and Phospholipid Membranes. *Langmuir* 34, 15084–15092.
- (50) Machinek, R. R. F., Ouldrige, T. E., Haley, N. E. C., Bath, J., and Turberfield, A. J. (2014) Programmable energy landscapes for kinetic control of DNA strand displacement. *Nat. Commun.* 5, 5324.
- (51) Di Michele, L., Moggetti, B. M., Yanagishima, T., Varilly, P., Ruff, Z., Frenkel, D., and Eiser, E. (2014) Effect of Inert Tails on the Thermodynamics of DNA Hybridization. *J. Am. Chem. Soc.* 136, 6538–6541.
- (52) Zadeh, J. N., Steenberg, C. D., Bois, J. S., Wolfe, B. R., Pierce, M. B., Khan, A. R., Dirks, R. M., and Pierce, N. A. (2011) NUPACK: Analysis and design of nucleic acid systems. *J. Comput. Chem.* 32, 170–173.
- (53) Talbot, E. L., Kotar, J., Parolini, L., Di Michele, L., and Cicuta, P. (2017) Thermophoretic migration of vesicles depends on mean temperature and head group chemistry. *Nat. Commun.* 8, 15351.
- (54) Liu, A., and Qi, X. (2012) Molecular Dynamics Simulations of DOPC Lipid Bilayers: The Effect of Lennard-Jones Parameters of Hydrocarbon Chains. *Comput. Mol. Biosci.* 2, 78–82.
- (55) Whitelam, S., and Geissler, P. L. (2007) Avoiding unphysical kinetic traps in Monte Carlo simulations of strongly attractive particles. *J. Chem. Phys.* 127, 154101.
- (56) Chodera, J. D. (2016) A Simple Method for Automated Equilibration Detection in Molecular Simulations. *J. Chem. Theory Comput.* 12, 1799–1805.